remote sensing

MDPI

Article

Ocean Oil Spill Classification with RADARSAT-2 SAR Based on an Optimized Wavelet Neural Network

Dongmei Song [1,2,*], Yaxiong Ding [1,3], Xiaofeng Li [4], Biao Zhang [5] and Mingyu Xu [1,3]

1 School of Geosciences, China University of Petroleum, Qingdao 266580, China; dyx_giser@163.com (Y.D.); z15010005@s.upc.edu.cn (M.X.)
2 Laboratory for Marine Mineral Resources, Qingdao National Laboratory for Marine Science and Technology, Qingdao 266071, China
3 Graduate School, China University of Petroleum, Qingdao 266580, China
4 GST at National Oceanic and Atmospheric Administration (NOAA)/NESDIS, College Park, MD 20740-3818, USA; xiaofeng.li@noaa.gov
5 School of Marine Sciences, Nanjing University of Information Science and Technology, Nanjing 210044, China; zhangbiao@nuist.edu.cn
* Correspondence: songdongmei@upc.edu.cn; Tel.: +86-150-630-10029

Academic Editors: Ali Khenchaf and Deepak R. Mishra
Received: 20 June 2017; Accepted: 1 August 2017; Published: 3 August 2017

Abstract: Oil spill accidents from ship or oil platform cause damage to marine and coastal environment and ecosystems. To monitor such spill events from space, fully polarimetric (Pol-SAR) synthetic aperture radar (SAR) has been greatly used in improving oil spill observation. Aiming to promote ocean oil spill classification accuracy, we developed a new oil spill identification method by combining multiple fully polarimetric SAR features data with an optimized wavelet neural network classifier (WNN). Two sets of RADARSAT-2 fully polarimetric SAR data are applied to test the validity of the developed method. The experimental results show that: (1) the convergence ability of optimized WNN can be enhanced, improving overall classification accuracy of ocean oil spill, in comparison to the classification results based on a common un-optimized WNN classifier; and (2) the joint use of the multiple fully Pol-SAR features as the inputs of the classifier can achieve better classification result than that only with single fully Pol-SAR feature. The developed method can improve classification accuracy by 4.96% and 7.75%, compared with the classification results with un-optimized WNN and only with one single fully polarimetric SAR feature. The classification overall accuracy based on the proposed approach can reach 97.67%. Experimental results have proven that the proposed approach is effective and applicable to classify the ocean oil spill.

Keywords: oil spill; wavelet neural network; fully polarimetric SAR; RADARSAT-2

1. Introduction

Oil spill happen often in the world oceans due to ship or oil platform accidents. They bring damage to coastal environment and marine ecosystems [1–4]. Satellite remote sensing technology has been widely used in oil spill observations due to its frequent large coverage and relatively low cost [5–11]. Among remote sensing sensors, synthetic aperture radar (SAR) can provide valuable synoptic information about the position and size of a particular oil spill under moderate wind speed (4–12 m/s) weather conditions, day and night [12]. However, it is a challenge to distinguish oil spills from other lookalike natural phenomena (biogenic slicks, upwelling, low wind areas, rain cells, shear zones, internal waves, etc.) in SAR images [13]. Efforts have been devoted to improve oil spill detection and classification. Nowadays, there is a general consensus that the extra information provided by the polarimetric SAR (Pol-SAR) data enhances the capabilities of identifying and classifying the

scattering behavior from different targets at sea [14–19]. A fully Pol-SAR transmits and receives two orthogonally polarized fields and, as a result, measures the scattering matrix for each resolution cell. Hence, this measurement process, considering the vectorial nature of the scattered field, retains all the information in the scattered electromagnetic wave describing the polarimetric properties of the observed scene [20–26]. Migliaccio used polarimetric decomposition theorem to show the polarimetric SAR approach is effective in oil spill detection [2]. Since then, many polarimetric models and signatures have been developed [7,8]. Some particular coefficients with fully polarimetric SAR for oil spill detection were proposed, such as conformity coefficient [15], co-polarized phase difference [7], pedestal height [21], Muller filter [24], degree of polarization [22] and geometric intensity and magnitude of co-polarization correlation coefficient [8]. However, from previous literature on identification or classification for ocean oil spill based on fully Pol-SAR feature, we find that scholars often employ a single fully Pol-SAR feature rather than multiple features. Table 1 summarizes most fully Pol-SAR features proposed by different scholars in recent years [26]. However, only using a single fully Pol-SAR feature might limit the improvement of classification performance. Therefore, the idea of joint use of multiple Pol-SAR features has been produced for the first time in this study to help enhance the classification performance.

Table 1. Most employed polarimetric features and their expected behavior over sea surface with and without slicks [26].

Pol-SAR Feature	Slick-Free Sea Surface/Lookalike	Oil Slice-Covered Sea Surface	References
H	Low	High	Migliaccio, Gambardella, and Tranfaglia (2007) [2], Migliaccio, Nunziata, Montuori, et al. (2012) [14], Minchew, Jones, and Holt (2012) [25]
A	Low	High	Minchew, Jones, and Holt (2012) [25], Skrunes, Brekke, and Eltoft (2014) [8]
A_{12}	High	Low	Skrunes, Brekke, and Eltoft (2014) [8]
$\overline{\alpha}$	Low	High	Minchew, Jones, and Holt (2012) [25]
ν	High	Low	Skrunes, Brekke, and Eltoft (2014) [8]
M_{33}	$\lvert {M_{33}}^{I} \rvert > \lvert {M_{33}}^{II} \rvert$	$\lvert {M_{33}}^{I} \rvert < \lvert {M_{33}}^{II} \rvert$	Migliaccio et al. (2011) [14]
μ	>0	<0	Zhang et al. (2011) [15], Skrunes Brekke, and Eltoft (2014) [8]
P	High	Low	Shivany, Chabert, and Tourneret (2012) [22]
P_{height}	Low	High	Nunziata, Migliaccio, and Gambardella (2011) [21]

Over the past several decades, artificial neural network algorithms have been widely used in remote sensing image classification [27–29], due to their good self-organization [30–32], self-learning [33,34], and self-adaptive abilities [35]. Among these, BP (Back Propagation) neural network is one of the first widely used network models due to its simple and easy to implement training in initially stage. Its network construction can realize mapping from the sample inputs to outputs through nonlinear relationship. In general, through iterative operation with gradient descent algorithm, the error of the network gradually decreases to tolerant range. However, BP algorithm also has shortcomings. It is a kind of local optimization search methods, and the calculation often does not converge, or converge to a local minimum. In addition, slow convergence calculation speed makes it only useful for solving small-scale problems. To overcome the deficiency of the BP network, wavelet neural network (WNN) was proposed [36]. WNN takes the topological structure of BP neural network as the basis of the network. The nonlinear function of BP neural network is replaced with the wavelet basis function. WNN combines time-frequency domain features of wavelet transform and self-learning ability of BP network. It effectively solves the BP neural network problem and has strong learning and generalization abilities. These advantages make WNN a widely applied method in remote sensing

image classification [37–39]. The initial value of WNN plays a key role in the neural network training process, and affects the network convergence nature and classification capability. In this study, we develop a method of setting better initial value for the WNN to improve SAR image classification performance to locate oil slicks.

The main objectives of this study are to: (1) demonstrate the capability and superiority of the combined utilization of multiple fully Pol-SAR features as the inputs of an classifier for ocean oil spill classification; and (2) indicate the superiority and effectiveness of an optimized WNN classifier in improving classification performance of ocean oil spills, compared with un-optimized WNN.

The remainder of this paper is organized as follows: In Section 2, RadarSat-2 Pol-SAR data used in this study and methodology are described; in Section 3, the experimental results are given. The discussion and the conclusions are given in Sections 4 and 5, respectively.

2. Data and Methodology

2.1. Remote Sensing Data

We used two sets of remote sensing data of fully Pol-Radarsat-2. Tables 2 and 3 present the information on the two RADARSAT-2 scenes and Figure 1 shows the images of the two sets of datasets used in this study. The product type is SLC (simple look complex). Both images are acquired in fine quad-polarization imaging in the Gulf of Mexico. The RADARSAT-2 fine quad-polarization imaging mode provides single-look complex data in HH, VV, HV, and VH channels with a low noise floor of −35 dB. The space resolution along azimuth directions and range directions are about 5 m. The range of the incident angle is 26.093° to 29.395° for Image 1, and 43.631° to 44.954° for Image 2. The place of study in Dataset 1 is SW of New Orleans in the northern Gulf of Mexico, near the mouth of the Mississippi River. The Mississippi River Delta can be seen obviously in the image.

Table 1 is a sectional table extracted from Reference [26], summarizing the behaviors of fully Pol-SAR features of seawater, lookalike and oil spill. According to the table, it can be known the pixel values of $\overline{\alpha}$ and H of oil spills are high, so their image tone should be brighter than the area covered by water or lookalike. On the contrary, the values of ν, μ, p and M33 of oil spill are low, therefore their image tone should be darker than the area covered by water or lookalike. According to this criterion [26], in terms of behavior of fully Pol-SAR features of an oil spill and water/lookalike, we can determine that the long strip objects in Dataset 1 and Dataset 2 in Figure 2, are oil spills, rather than lookalikes.

Table 2. Information on the image of RadarSAT-2 used in this study (Dataset 1).

Product Type	SLC (Single Look Complex)
Start Time	2015-05-08 T 23:53:36
Beam Mode	FQ8W
Polarization	HH VV HV VH
Look Direction	Right
Pixel Spacing	4.73 m × 4.78 m
Incidence Angle	2.60E1~2.93E1
Area Covered	32.95 km × 23.2 km

Table 3. Information on the image of RadarSAT-2 used in this study (Dataset 2).

Product Type	SLC (Single Look Complex)
Start Time	2011-06-17 T 11:48:20
Beam Mode	FQ25
Polarization	HH VV HV VH
Look Direction	Right
Pixel Spacing	4.73 m × 5.05 m
Incidence Angle	4.36E1~4.49E1
Area Covered	37.17 km × 19.34 km

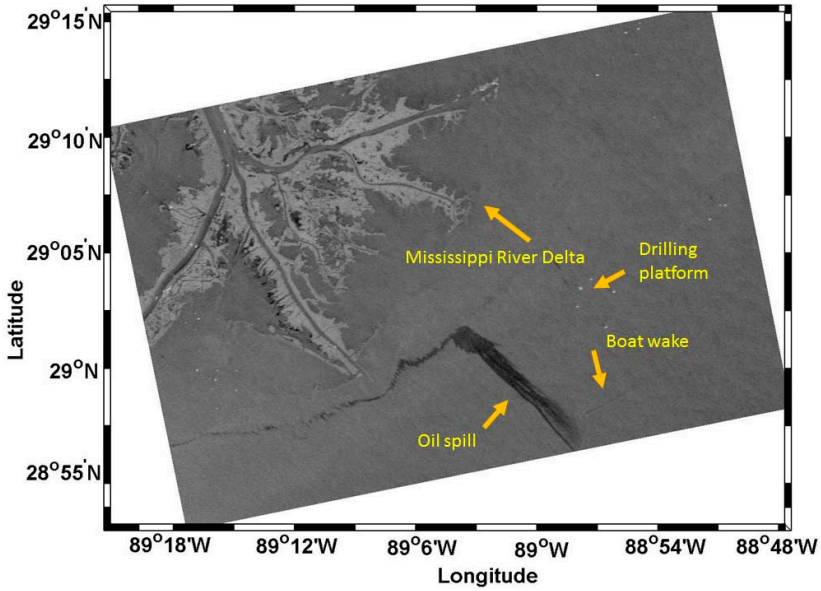

(**a**)

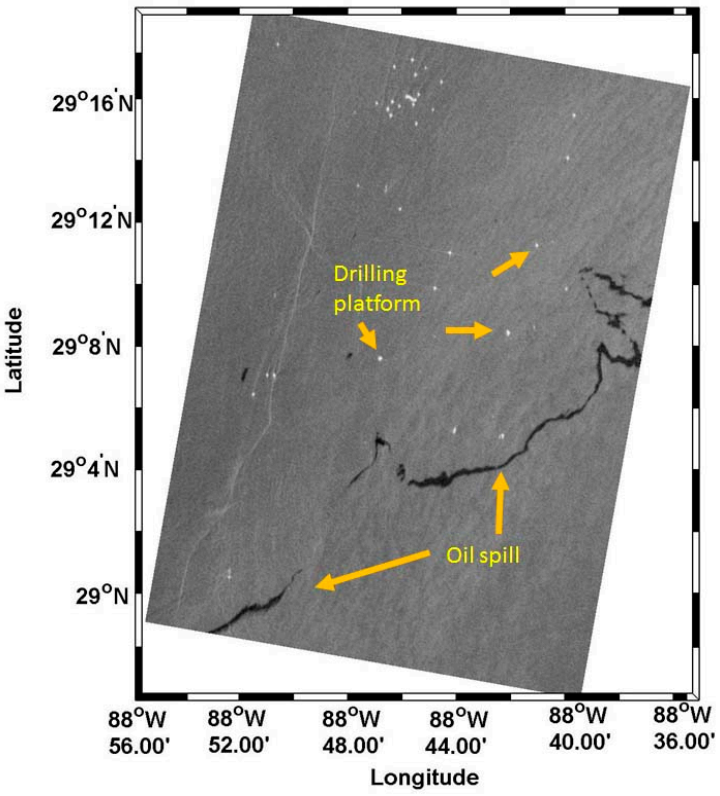

(**b**)

Figure 1. The ocean oil spill image of RadarSat-2 in fine quad-polarization imaging mode used in this study: (**a**) oil spill image of RadarSat-2 SAR (Dataset 1); and (**b**) oil spill image of RadarSat-2 SAR (Dataset 2). There are oil spill, water, island, and oil platform in the image of Dataset 1, and there are oil spill, water and oil platform in the image of Dataset 2.

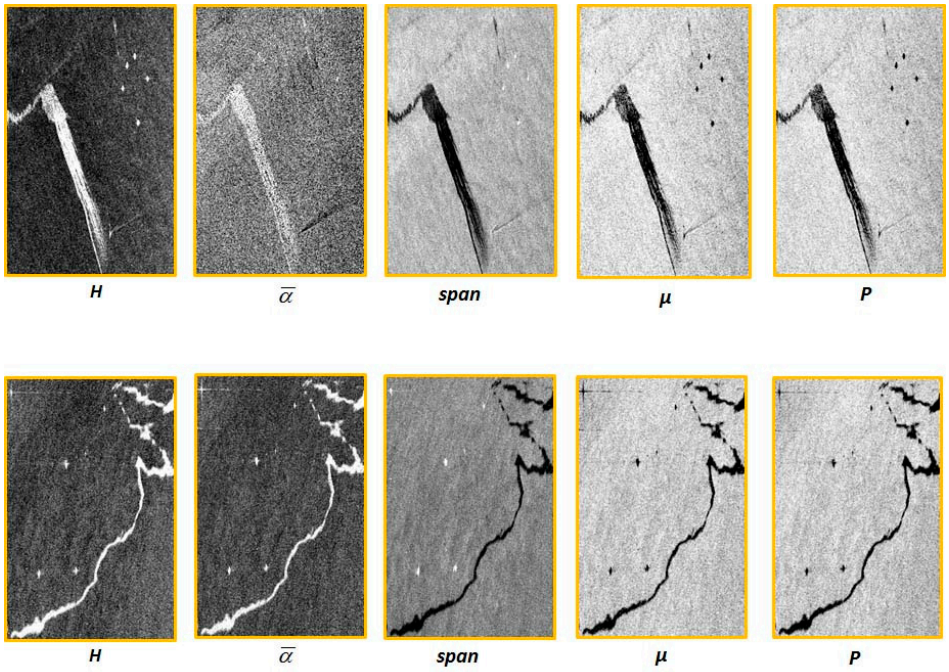

Figure 2. Presentation of several fully Pol-SAR features of Dataset 1 and Dataset 2.

2.2. Introduction of Method Frame for Classifying the Ocean Oil Spills from Water

Figure 3 demonstrates the scheme of the proposed method. The method includes two main parts. The first main part is about the selection process of the fully Pol-SAR features based on the *J-M* distance index method, extracted from RadarSAT-2 SAR data. The selected features will be used as the inputs of an optimized classifier. The process is explained in detail in Section 2.2.2. The second key part of the proposed method is an introduction about developed optimized wavelet neural networks (WNN) classifier. The optimization processing of the classifier is exhibited in Section 2.2.3. Oil spill classification results will be generated based on the optimized WNN classifier with the multiple selected fully Pol-SAR features. Classification accuracy will be assessed and compared with these based on: (1) un-optimized WNN classifier; and (2) single fully Pol-SAR feature. The effectiveness of the proposed method will be estimated in Section 4.

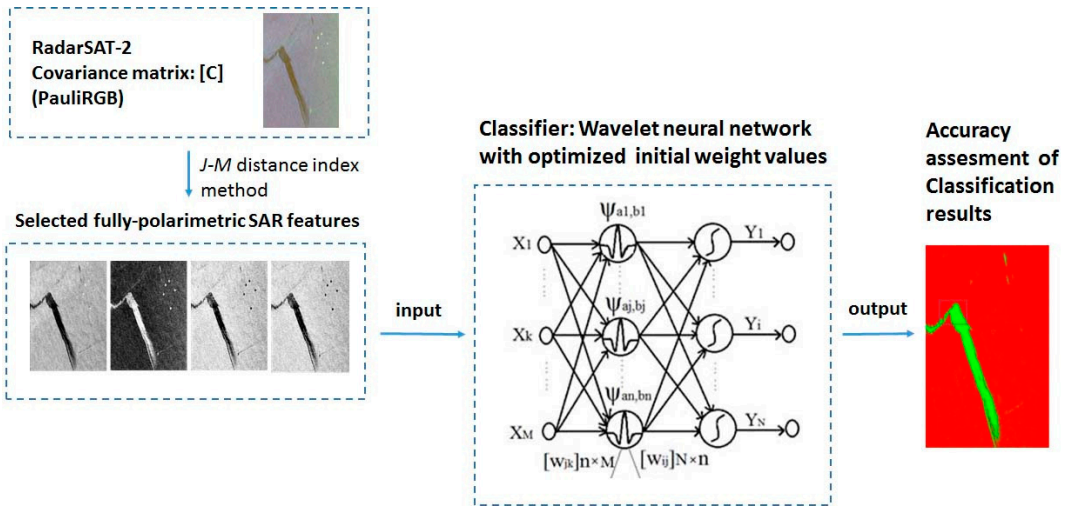

Figure 3. Frame chart of experimental process for ocean oil spill classification.

2.2.1. The Combination of Multiple Fully Pol-SAR Features for Improving Ocean Oil Spill Identification

The ground object classification in remote sensing imagery is based on the difference of its feature values. Generally, the feature pixel values of the same object are similar; on the contrary, different objects possess different feature values. Therefore, the pixels of the same object present gathered and cluster characteristic and hold certain area coverage, while different objects occupy different areas in the feature space (shown in Figure 4). The more different the feature value of each object is, the higher the probability of being accurately classified is each object. Although the feature value of the most of pixels of different objects are separate in feature space, there is always observed mixture phenomenon of feature value of few pixels of different objects. As shown in Figure 4, feature values of most oil and water pixels are separate, but there are still a few cross-mixed regions of pixels, marked as the red border.

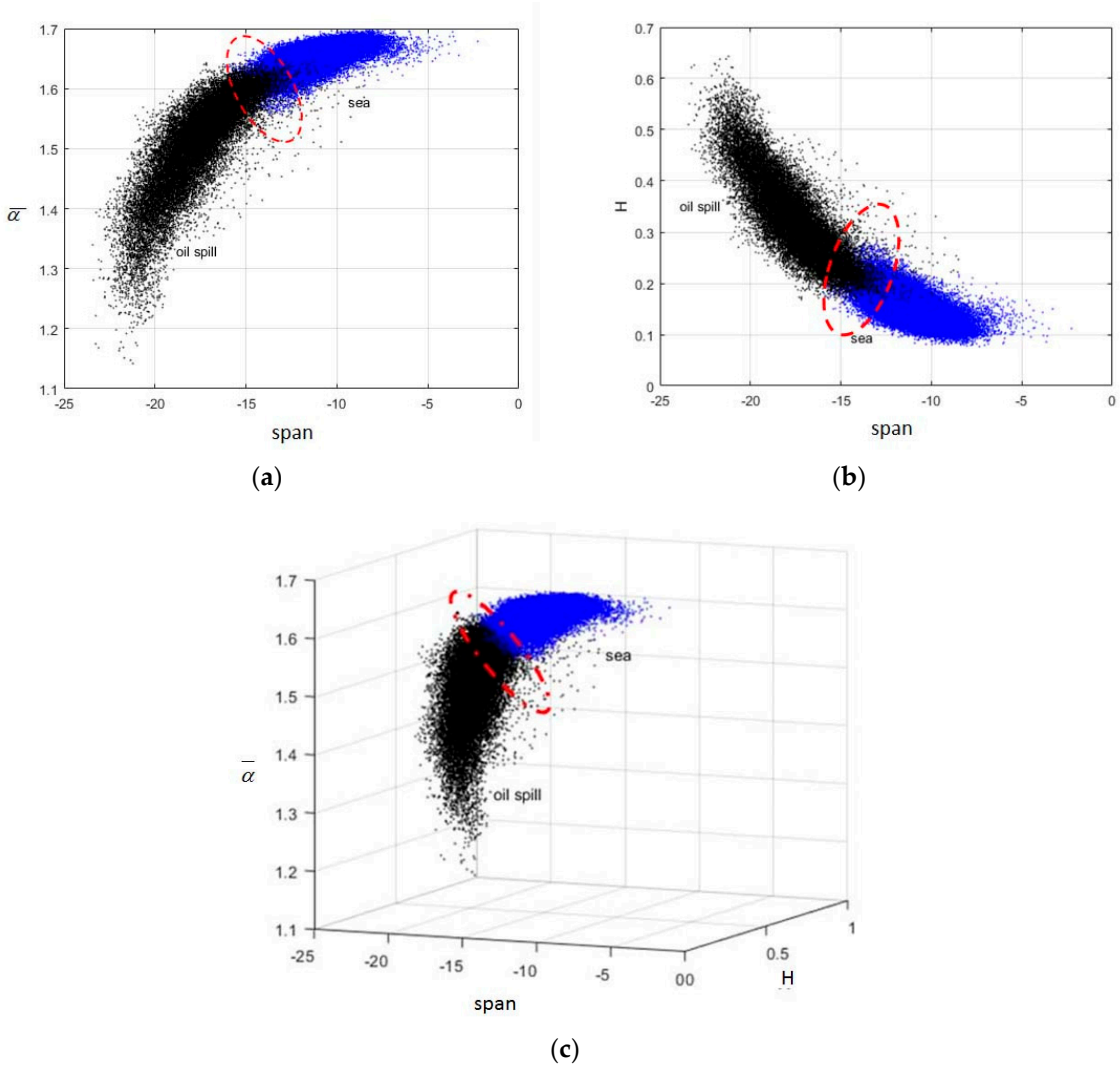

Figure 4. Clusters of ocean oil spill and water in region of interesting in two and three dimensional feature space: (**a**) *span-*$\overline{\alpha}$; (**b**) *span-H*; and (**c**) $\overline{\alpha}$*-span-H*.

Figure 5 shows the probability density distribution of pixels feature value between ocean oil spill and water in region of interest (ROI) in the case of one-dimensional feature space. The overlaid area shows the cross-mixed phenomena. The X-axis is the feature value, and the Y-axis is the number of pixels under the corresponding feature value. Figure 5a,b shows Span, and H of fully Pol-SAR features

derived from the RadarSAT-2 Dataset 1. The peak value of probability density of oil spill and water is separated entirely, which illustrates that Span and H are effective features. However, the cross section of curve in the red border of the probability density figure displays the cross-mixed phenomena of feature value of pixels between oil spills and water in a one-dimensional feature space. This indicates using any single fully Pol-SAR feature we will inevitably make some misclassification for oil spill and water which pixels features point clusters locate in overlaid area in feature space. Therefore, the threshold segmentation method based only on a single feature value for identifying the oil spills from water will almost surely cause segmentation error. The probability of wrong classification is related to mix degree of oil spills and water in the feature space.

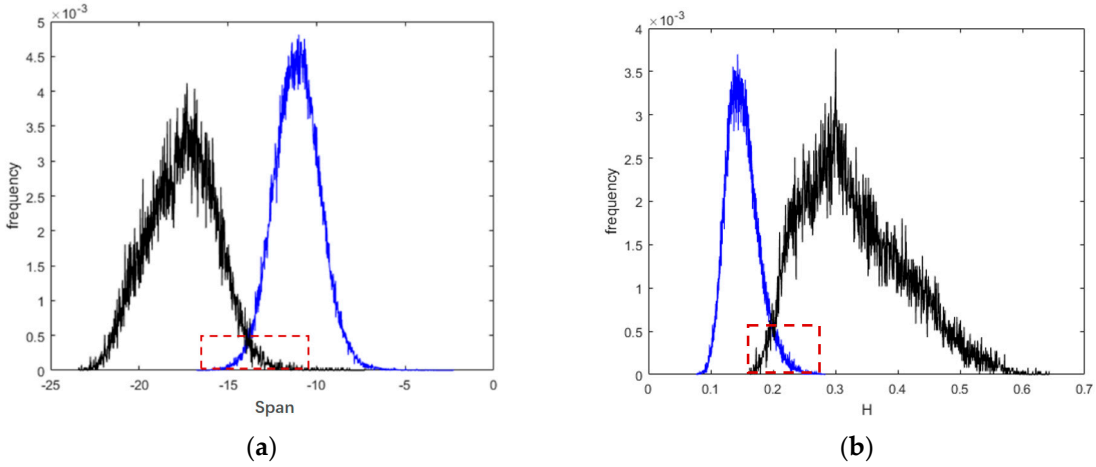

Figure 5. Probability density of ocean oil spill and water in region of interesting in one dimensional feature space: (**a**) *span*; and (**b**) *H*.

However, when we add more Pol-SAR parameters in classification process, those pixels in the mixture cluster in feature space will reduce when finding a suitable segmentation curved surface, hence they will obtain more chances to be classified to the correct object types. This is because a higher separation ability will be achieved in higher dimensional feature space than that in a one-dimensional feature space, according to the knowledge of feature classification [40–42], such as in the classification process for sea ice with Pol-SAR data [41,42], multiple features are often employed to classify the objects, rather than only depending on a single feature. Therefore, we naturally generate an idea that, when making classification of ocean oil spill with fully Pol-SAR data, multiple features should be jointly used to try to enhance the classification performance, since we have obtained many types of fully Pol-SAR features of oil spill proposed by different scholars. For example, Figure 6 exhibits the different ability of identifying the oil spill from other objects based on several Pol-SAR features. In Figure 6a, the objects in the region of the "a" are drilling platform. It has similar image tone with the oil spill, consequently it is difficult to classify them. However, in Figure 6b,c, it is very easy to identify oil spill from the drilling platform shown in areas "b" and "c", since they have a contrary image tone, compared with the oil spill. In the same way, the object in areas "d", "e", and "f" is the wake of a boat. In Figure 6a,c, the oil spill and boat wake have a similar tone, so it is hard to correctly classify them, whereas, when introducing the image of Figure 6b, the problem is easily solved, since the boat wake has different image tone, compared with the image tone of oil spill. As a whole, Figure 6a–c presents a visualized behavior of oil spill and water/lookalike in different fully Pol-SAR features. By analyzing the characteristic of different objects in different fully Pol-SAR features images, we can be convinced of jointly usage of multiple fully Pol-SAR features can really improve the identifying ability of oil spill from water or lookalike, like the wake of a boat, and some other objects, such as the drilling platforms.

Figure 6 effectively proves the necessary of combined use of multiple fully Pol-SAR features for oil spill classification.

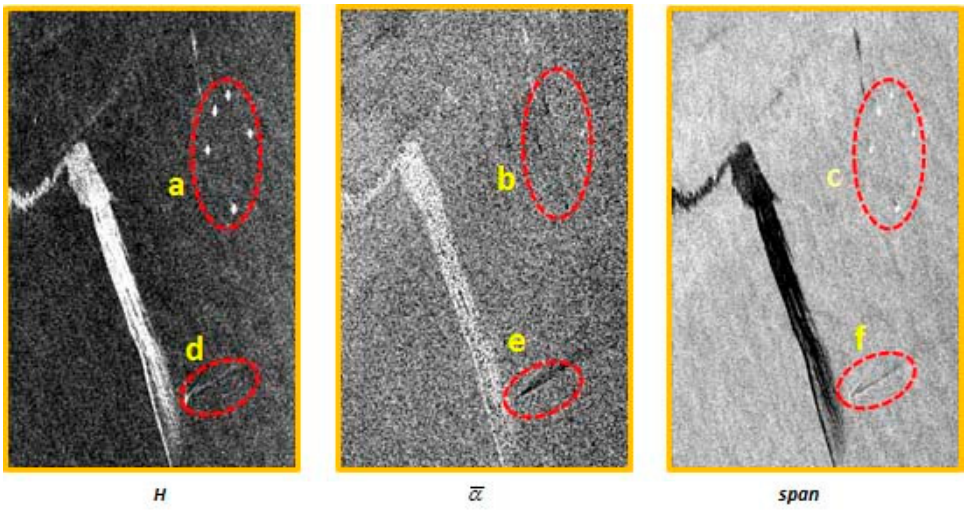

Figure 6. The difference of identifying ability of oil spill from the boat wake and drilling platforms based on several fully Pol-SAR features extracted from Dataset 1. (**a**) the image of fully Pol-SAR feature H (polarization entropy); (**b**) the image of fully Pol-SAR feature $\overline{\alpha}$ (mean scattering angle); (**c**) is the image of fully Pol-SAR feature span (backscattered energy).

2.2.2. Selection Criteria of Fully Pol-SAR Features Based on J-M Distance Method

For adequately exploiting the advantages of joint usage of multiple fully Pol-SAR features for oil spill classification, we first need to determine optimal combination pattern of multiple features. It is not necessary for every single Pol-SAR feature to be used in the classification process. The commonly used fully Pol-SAR features for oil spill detection include *span* [8], ρ [7], H [1], A [25], $\overline{\alpha}$ [25], μ [15], and P [22]. Each of these features has its own different ability for identifying the ocean oil spills from water. To achieving joint use of fully Pol-SAR features, we have to employ feature selection method to determine combination pattern of fully Pol-SAR features. Jeffreys–Matusita distance (*J-M*) is an index that is widely used to select useful features [43]. The chosen features will be as the inputs of the WNN in this study. The calculation of the index is simple and has good universality [43]. The calculation method of *J-M* distance of two different objects (oil and water) with a feature is shown in Equations (1) and (2):

$$J = 2(1 - e^{-B}) \tag{1}$$

$$\mathrm{B} = \frac{1}{8}(m_1 - m_2)^2 \frac{2}{\delta_1^2 + \delta_2^2} + \frac{1}{2}\ln\left[\frac{\delta_1^2 + \delta_2^2}{2\delta_1\delta_2}\right] \tag{2}$$

where J represents *J-M* distance index under a certain feature, such as *span* or μ in this study. m_1 and m_2 are mean of a certain feature value of two kinds of different ground objects, respectively. In this study, m_1 and m_2 are mean of the feature value of oil spill and water. δ_i and δ_i are the deviation of a certain feature value of oil spill and water, respectively. The value range of J is 0–2. When the value of the J is 0–1, the two objects have weak separability under a certain feature. When J is 1–1.9, the two objects have a certain separability under a certain feature. When $J > 1.9$, the two objects have strong separability under a certain feature [44].

Calculation result of *J-M* index based on the feature value demonstrates that *span*, H, μ , $\overline{\alpha}$, and P all have higher separability ability for identifying the ocean oil spills from water, because the value

of *J* index is greater than 1.5. Therefore, these features are used in this classification experiments. The calculations of these features are summarized in Table 4.

J-M distance indexes are shown in Figure 7. Four fully Pol-SAR features (*span*, *H*, μ, and *P*) are selected for Dataset 1 (solid line), while the other four ($\overline{\alpha}$, *H*, μ, and *P*) are selected for Dataset 2 (dash line), as these *J-M* distance indexes are similar to or greater than 1.5. Therefore, five selected features (*span*, *H*, μ, *P* and $\overline{\alpha}$) have certain identification ability for separating oil spill from water.

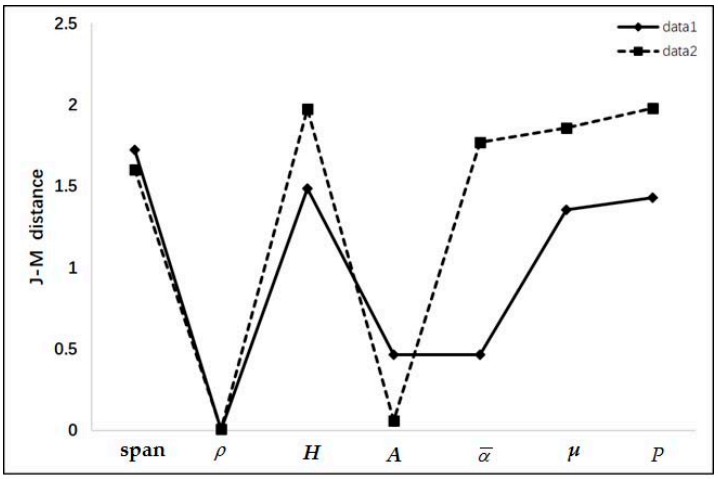

Figure 7. *J-M* distance index of different fully Pol-SAR features of Dataset 1 and Dataset 2. span: backscattered energy [8]; ρ: co-polarized complex correlation [7]; H: polarization entropy [1]; A: anisotropy coefficient [25]; $\overline{\alpha}$: mean scattering angle [25]; μ: conformity coefficient [15]; P: degree of polarization [22].

Table 4. Introduction of selected full pol-SAR features used in this study.

Feature	Formula	Symbol	Characterization
span	$span = \lvert S_{hh}\rvert^2 + \lvert S_{hv}\rvert^2 + \lvert S_{vh}\rvert^2 + \lvert S_{vv}\rvert^2$	S_{xy}: represents scattering amplitudes	the total power of SAR scattering target
H	$H = -\sum_{i=1}^{3} p_i \log_3 p_i$ $p_i = \frac{\lambda_i}{\sum_{i=1}^{3}\lambda_i}$	λ_i: weight of corresponding scattering mechanisms p_i: pseudo-probability	characterizes the degree of randomness of the polarimetric scattering behavior
μ	$\mu \cong \frac{2\left(\Re(S_{hh}S_{vv}^*) - \lvert S_{hv}\rvert^2\right)}{\left(\lvert S_{hh}\rvert^2 + 2\lvert S_{hv}\rvert^2 + \lvert S_{vv}\rvert^2\right)}$	S_{xy}: element of scattering matrix $\Re$: real part	represents the different scattering mechanism
P	$p = \frac{\sqrt{s^s(2)+s^s(3)+s^s(4)}}{s^s(1)}$	$S^s(i)$: element of scattered Stokes vector	characterize that how close the scattering mechanism of the observed scene is to be deterministic
$\overline{\alpha}$	$\overline{\alpha} = \sum_{i=1}^{3} p_i \alpha_i$	α_i: phase related to each scattering mechanism	describes the scattering mechanism that characterizes the observed scene

Figure 2 shows the images of chosen fully Pol-SAR features. We can intuitively see the difference of image tone of oil spill and water; hence, we believe the chosen features have good classification ability. Meanwhile, the edge of the oil spills, such as the bottom pixels of the oil spills of Dataset 1, present weak contrast with water. Classification that only depends on one or two fully Pol-SAR feature images will inevitably cause segmentation error. The combined usage of the multiple fully Pol-SAR feature images are necessary to help improve the classification performance of oil spills and water.

As a general view, the chosen fully Pol-SAR features are effective for oil spill classification, in terms of the feature images contrast degree (shown in Figure 2). These selected features will all be used as the inputs of the optimized WNN classifier, and for conducting the training of neural network.

2.2.3. Optimization Strategy of the Initial Value of Wavelet Neural Network

In Section 2.2.2, we explain the selection method of fully Pol-SAR features based on the J-M distance index. These features are span, H, μ and P for the classification experiment with Dataset 1, and $\overline{\alpha}$, H, μ, and P for the classification experiment with Dataset 2. The selected features will be as the inputs of the optimized WNN classifier, guiding the training process of the neural network. In Section 2.2.3, we introduce the optimization strategy of the WNN. In Section "The Architecture of the Wavelet Neural Network", we firstly exhibit the architecture of the WNN. Then, in Section "Optimization Method of the WNN", we present the optimization process of WNN.

The Architecture of the Wavelet Neural Network

The WNN applied in this study includes an input layer, a hidden layer, and an output layer. A corresponding weight value matrix is used for connecting the input layer with the hidden layer, and the hidden layer with the output layer. The WNN architecture with a single hidden layer is shown in Figure 8.

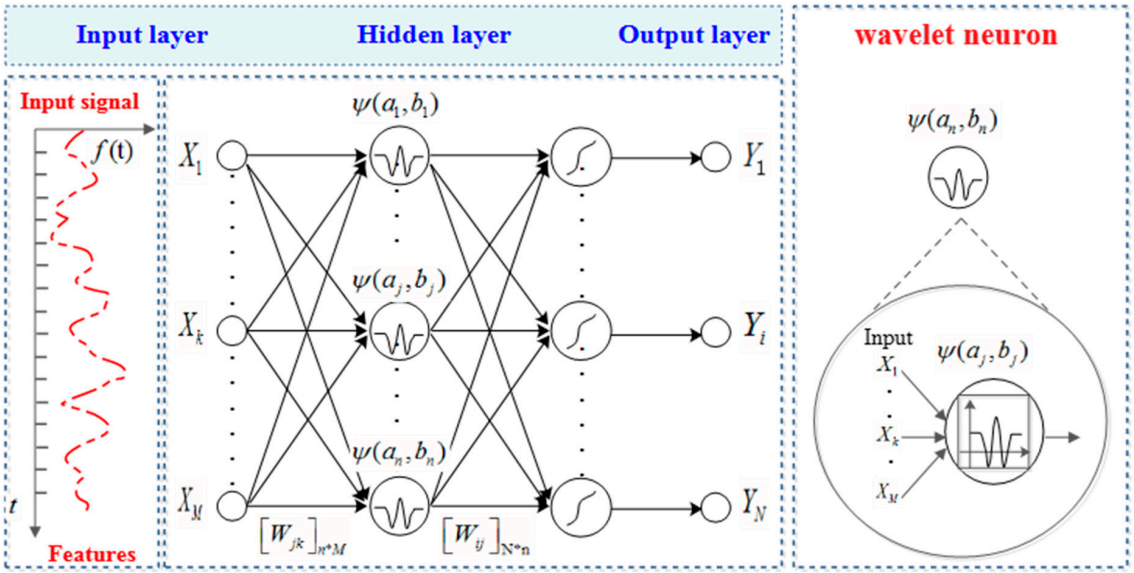

Figure 8. Wavelet neural network architecture with a single hidden layer.

The excitation function of the hidden layer of the WNN uses the Morlet wavelet function (see Formula (3)).

$$\psi(t) = e^{(-\frac{t^2}{2})} \cos(1.75t) \tag{3}$$

The wavelet neural network model is constructed by Equations (4)–(7).

$$net_j^p = \sum_{k=1}^{M} w_{jk} x_k^p \tag{4}$$

$$\psi_{a,b}(net_j^p) = \psi(\frac{net_j^p - b_j}{a_j}) \tag{5}$$

$$y_i^p = f[\sum_{j=1}^{n} w_{ij} \psi_{a,b}(net_j^p) - \beta_i],\ i = 1, 2, \cdots, n \tag{6}$$

$$net_i^p = \sum_{j=1}^{n} w_{i,j} \psi_{a,b}(net_j^p) \quad (7)$$

The meaning of the parameters is summarized in Table 5.

Table 5. The definition of parameters used in Equations (4)–(7).

Parameter	Definition
$p(p = 1, 2, \cdots, P)$	number of input samples
$k(k = 1, 2, \cdots, M)$	number of nodes in the input layer
$j(j = 1, 2, \cdots, n)$	number of nodes in the hidden layer
$i(i = 1, 2, \cdots, N)$	number of nodes in the output layer
$[w_{jk}]_{n \times M}$	weight matrix $n \times M$ from the input layer to the hidden layer, with w_{jk} as the weight connecting node j of hidden layer with the node k of the input layer); (the initial value is a random value of −1–1)
$[w_{1j}]_{N \times n}$	weight matrix $N \times n$ from the hidden layer to the output layer, with w_{ij} as the weight connecting the node i of the output layer and node j of the hidden layer; (the initial value is a random value of −1–1)
x_k^p	The kth input of the pth sample in the input layer
net_j^p	input of the jth node in the hidden layer of the pth sample
net_i^p	input of the ith node in the output layer of the pth sample
a_j and b_j	scaling parameter and translation parameter of the jth node of the hidden layer, respectively
$\psi_{a,b}(net_j^p)$	output of the jth node of the hidden layer of the pth sample
β_i	threshold value at the ith node of the output layer, (the initial value is a random value of −1–1)
y_i^p	the ith actual output in the output layer of the pth sample

Optimization Method of the WNN

The initial value of WNN plays an important role in train process of a network. A good initial value can improve the convergence speed and classification accuracy of a network. The nature of optimization method of the initial value of a WNN network proposed in this paper is obtaining a set of optimal initial value for the classifier, by making use of the relationship between the initial value (W_{jk}, a_i, b_i) of a WNN and training samples of ROI. The detailed steps are as follows:

Step 1 Set up the initial value of W_{jk}.

Firstly, a random number of 1–1 is generated as the initial value of W_{jk}. Then, W_{jk} is normalized according to the Equation (8).

$$W_{jk} = \frac{W_{jk}}{\sqrt{\sum_{k=1}^{M} W_{jk}^2}} \; j = 1, 2, \cdots, n \quad (8)$$

Next, W_{jk} is calculated. The function is given by Equations (9) and (10)

$$W_{jk} = C \cdot n^{\frac{1}{m}} \cdot W_{jk} \; j = 1, 2, \cdots, n \quad (9)$$

$$W_{jk} = \frac{2W_{jk}}{x_{k\max} - x_{k\min}} \; j = 1, 2, \cdots, n \quad (10)$$

where M is the number of the input layer nodes. n is the number of the hidden layer nodes. C is a constant. $\chi_{k\max}$ is the maximum value of the input samples of the ith neuron node of the input layer. $\chi_{k\min}$ is the minimum value of the input samples of the ith neuron node of the input layer.

Step 2 **Calculate the initial value of a_i** (Scaling parameter of the jth node of the hidden layer). The function is given by Equation (11)

$$a_i = \left(\sum_{j=1}^{M} x_{j\max} - \sum_{j=1}^{M} x_{j\min} \right) \div (0.7 \times \Delta x_{0i}) \tag{11}$$

where Δx_{0i} is the width of the window. $x_{j\max}$ is the maximum value of the input samples of the jth neuron node of the input layer. $x_{j\min}$ is the minimum value of the input samples of the jth neuron node of the input layer.

Step 3 **Calculating the initial value of b_i** (translation parameter of the jth node of the hidden layer). The function is given by Equation (12)

$$b_i = 0.5 \times \left(\sum_{j=1}^{M} x_{j\max} + \sum_{j=1}^{M} x_{j\min} \right) - a_i \times x_{0i} \tag{12}$$

where the meaning of $x_{j\max}$, $x_{j\min}$ and Δx_{0i} are the same as above-mentioned explained.

The classification process of the WNN in this experiment is as shown in Figure 9. The process is explained in detail as follows:

Step 1 **Implement the preprocessing of the original image.** The Pol-SAR features are extracted, and the expert interpretation map is determined. The region of interest is selected.

Step 2 **Build the WNN model**. The number of nodes in each layer is determined. Numbers of the input layer nodes equal to numbers of the selected features (in Dataset 1 experiment, *span*, H, μ, and P fully Pol-SAR features are selected, and, in Dataset 2 experiment, $\overline{\alpha}$, H, μ, and P features are selected by *J-M* index). Numbers of hidden layer nodes are determined by the testing. In this study, we set the number of the hidden layer nodes as 15, 20, 25, 30, 35, and 40 to evaluate the convergence and classification performance under different neural network structure. The numbers of output layer nodes is equal to the number of classified types. In this study, the classified types are oil spill and water, the number of the output layer nodes is 2.

Step 3 **Train the wavelet neural network.** The pixel values of the selected fully Pol-SAR features (*span*, H, μ, and P of Dataset 1; $\overline{\alpha}$, H, μ, and P of Dataset 2) in the region of interest are used as the input of the WNN to conduct the training of the network. The number of iterations is set to 100. The minimum output error E_{min} of the neural is set to 1×10^{-5}. If the output error $E < E_{min}$, then the training iteration ends. If $E > E_{min}$, then the training iteration continues.

Step 4 **Obtain the classification results.**

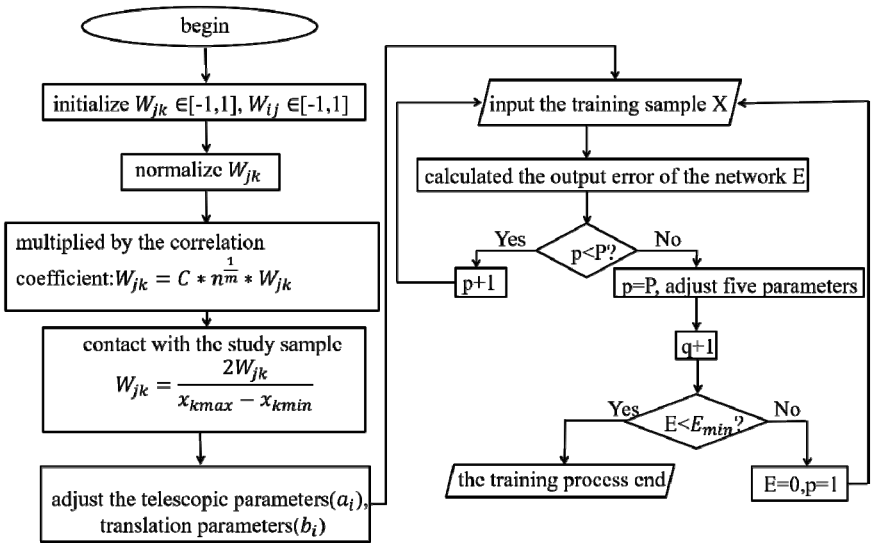

Figure 9. Flow chart for the training process of the wavelet neural network.

3. Result

3.1. Classification Result and Accuracy Analysis

The ocean oil spill classification results of experiments of Dataset 1 and Dataset 2 are summarized in Tables 6 and 7, respectively. Table 6 shows the classification results with different Pol-SAR features based on optimized and un-optimized WNN of the experiment of Dataset 1. On the one hand, the combined usage of four features (μ, P, H, and *span*) has highest classification accuracy in the case of same classifier, compared to single Pol-SAR feature. Classification accuracy of optimized WNN with four features as the input of the network arrives to 96.55%, and Kappa coefficient is 0.936. The classification accuracy of four Pol-SAR features is improved by 7.75%, 5.79%, 3.7% and 2.13%, compared to the classification results only using single μ, P, H, and *span* as the input of the optimized classifier, respectively. The classification accuracy of four Pol-SAR features is improved by 3.65%, 3.12%, 3.91% and 0.65%, compared with the classification results, only applying μ, P, H, and *span* as the input of un-optimized classifier, respectively. This result proves that the four Pol-SAR features as the network input can effectively improve the classification ability. On the other hand, when the input feature is the same, optimized WNN classifier always has higher classification ability than that of un-optimized classifier regardless of which one feature is as the input. Classification accuracy of optimized classifier with four features μ, P, H, and *span* feature is improved by 4.65%, 0.55%, 1.98%, 4.86%, and 3.17%, respectively, compared with the classification accuracy of un-optimized classifier. It indicates that optimal WNN has better enhanced the classification accuracy. When observing the convergence times, it can also be seen the superiority of optimized classifier, in comparison to the un-optimized classifier.

Table 6. The experimental results of Dataset 1.

Input(s)	Training Samples	Testing Samples	Optimized WNN			Un-Optimized WNN		
			OA (%)	Kappa	Convergence Rate	OA (%)	Kappa	Convergence Rate
Four features	600	2000	**96.55**	**0.936**	**174/180**	91.90	0.877	149/180
μ	500	2000	88.80	0.876	155/180	88.25	0.810	105/180
P	500	2000	90.76	0.854	151/180	88.78	0.840	107/180
H	500	2000	92.85	0.860	170/180	87.99	0.842	108/180
span	500	2000	94.42	0.827	109/180	91.25	0.841	107/180

Note: OA is the overall accuracy of classification; Kappa is the meaning of Kappa coefficient.

Table 7. The experimental results of Dataset 2.

Input(s)	Training Samples	Testing Samples	Optimized WNN			Un-Optimized WNN		
			OA (%)	Kappa	Convergence Rate	OA (%)	Kappa	Convergence Rate
Four features	600	2000	**97.67**	**0.948**	**153/180**	92.71	0.877	135/180
μ	500	2000	92.56	0.871	145/180	91.66	0.810	101/180
P	500	2000	95.05	0.854	151/180	92.10	0.840	103/180
$\boldsymbol{H}$	500	2000	94.10	0.860	170/180	92.64	0.842	110/180
$\overline{\alpha}$	500	2000	93.29	0.827	113/180	91.31	0.841	102/180

Note: OA and Kappa have the same meaning as above table.

Table 7 shows the classification results of the Dataset 2. It also shows that the optimized wavelet neural network has great ability of enhancing the classification accuracy. As a whole, the classification results of Dataset 1 and Dataset 2 manifest that the combined usage of multiple fully Pol-SAR features and the optimal classifier can greatly improve classification accuracy of ocean oil spill.

3.2. *Effect of Different Numbers of Hidden Layer Nodes on WNN Classification Performance*

Figures 10 and 11 demonstrate the classification results of Image 1. Figure 10 shows the mean of overall accuracy (OA) and kappa coefficient of 30 times of tests of Dataset 1 with the optimized WNN and un-optimized methods. The optimal WNN is obviously superior to the un-optimized WNN. No matter how many hidden layer nodes of the WNN, the optimized method has higher average classification accuracy. Meanwhile, the un-optimized WNN presents obvious fluctuation in classification accuracy. Especially when the number of the hidden layer nodes is 15, 20, 25, and 30, the OA of classification shows strong fluctuation. When investigating the convergence of these two classifiers, we can see that 30 times of classification tests of the optimized classifier are all convergent. However, the un-optimized WNN did not converge twice when hidden layer node is 25 and 30. The experimental results of Dataset 1 show that the optimized classifier has better and stable classification ability.

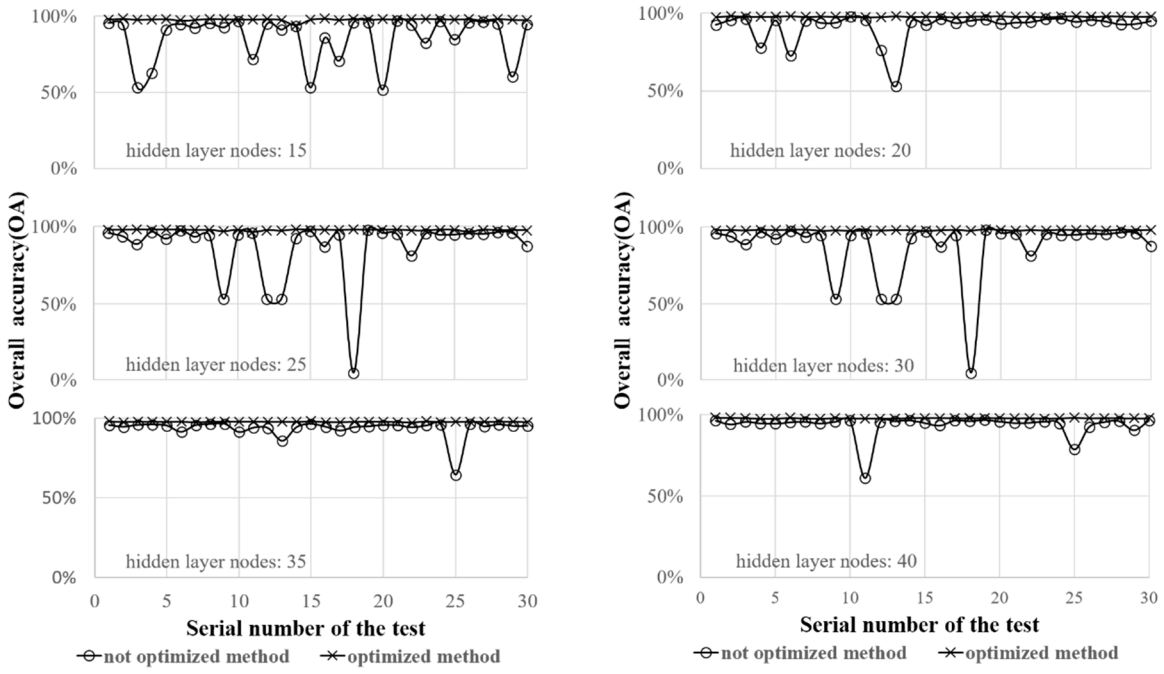

Figure 10. Classification overall accuracy of optimized and un-optimized WNN with different hidden layer nodes of Dataset 1.

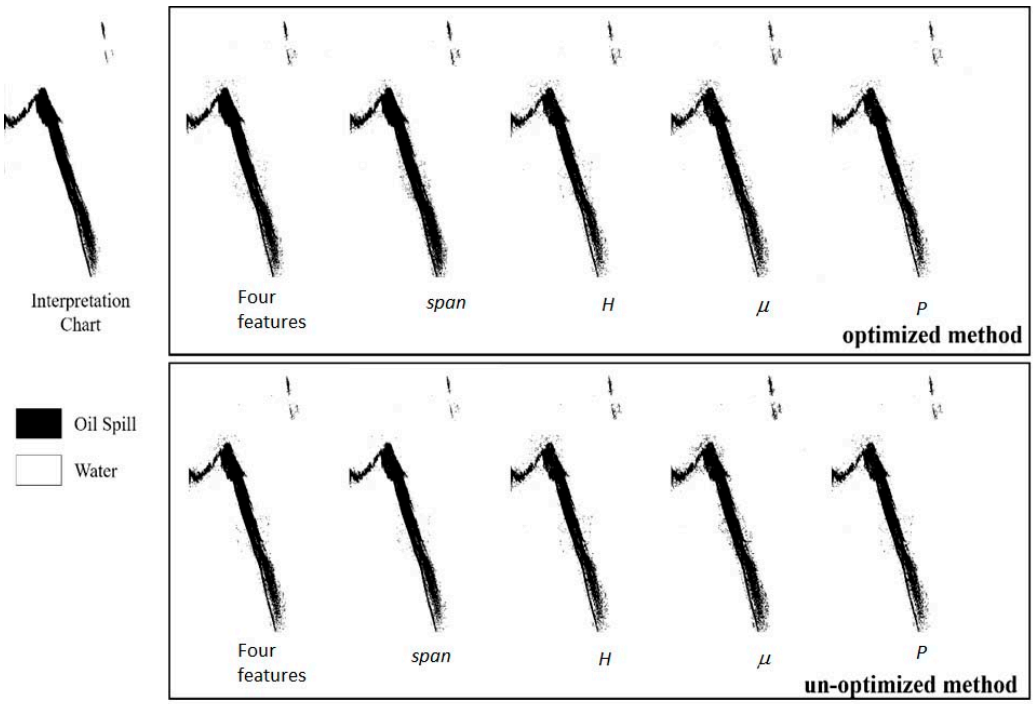

Figure 11. Classification results of Dataset 1.

Figures 12 and 13 show experimental results of Dataset 2. Figure 12 also indicates the optimized classifier has higher average classification accuracy. However, we can see that the classification accuracy of optimized method presents three times vibrate state when the hidden layer node is 35. In the case of other hidden layer node, the OA of classification of optimized network is always better than that of the un-optimized network. In short, the experimental results of Dataset 2 also show that optimized WNN classifier has better and stable classification ability.

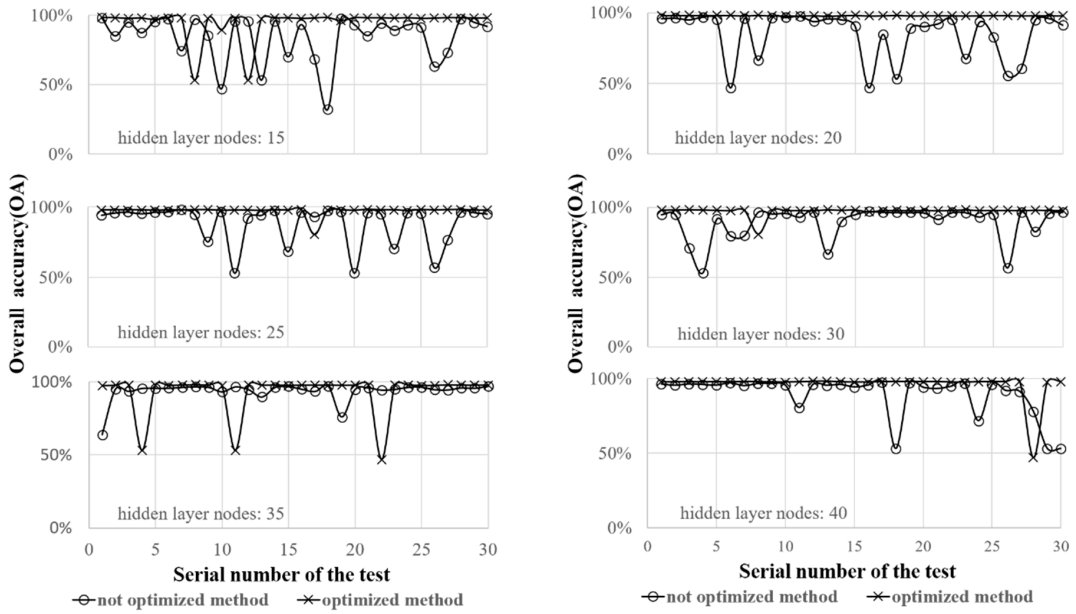

Figure 12. Classification overall accuracy of optimized and un-optimized WNN with different hidden layer nodes of Dataset 2.

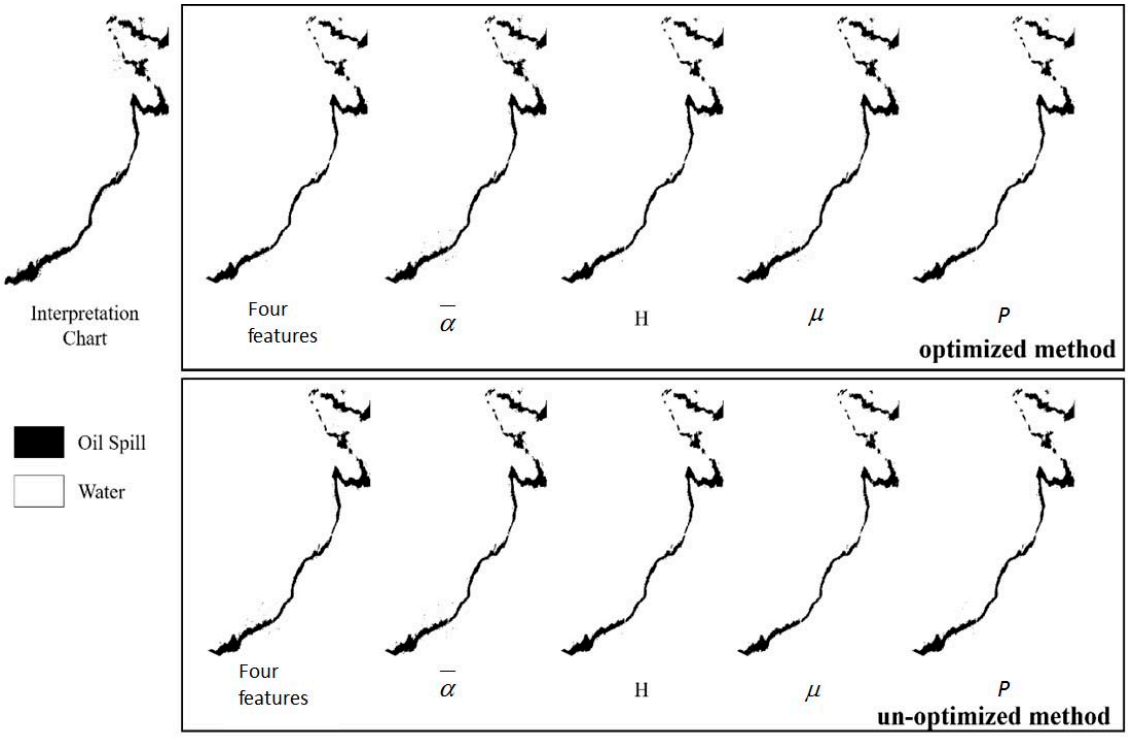

Figure 13. Classification results of Dataset 2.

4. Discussion

4.1. Combination Pattern of Pol-SAR Features for Oil Spill Classification Should Be Taken into Consideration

Quad-polarization SAR measures the scattering matrix and provides full amplitude and phase information of each image pixel [7]. In land-use classification, previous studies show that quad-polarization SAR data yield more useful information than conventional single-polarization SAR [7,8]. RADARSAT-2 quad-polarization (HH, HV, VH, and VV) SAR measures the scattering matrix of each SAR image pixel. The measurement retains all the information describing the polarimetric properties of the observed scene in the scattered field. Due to the vector nature of the scattered field, quad-polarization measurements can be used to classify SAR imagery with different scattering mechanisms [8,15]. However, previously, most research on the identifying of ocean oil spill from the water was based only on a single fully Pol-SAR feature, which would inevitably limit the enhancement of classification accuracy. Therefore, in this study, combined use of multiple fully Pol-SAR features for oil spill classification has been suggested and proved it can improve the classification ability, compared with only a single feature. Combination pattern of joint use of several fully Pol-SAR features should be discussed and investigated carefully in further research. Although in this study with two sets of RADARSAT-2, the five fully Pol-SAR features are successfully selected by *J-M* distance method and proved effectiveness of improving classification performance of ocean oil spill, when applying the other fully Pol-SAR datasets, or when there are other lookalikes in SAR imagery, effective combination pattern of fully Pol-SAR features might vary. The reason is that the types of oil spill and variable ocean environment, such as the wind speed change, may result in changing of effective combination pattern. Consequently, different methods for selecting features are suggested to be tested to determine effective combination pattern of fully Pol-SAR features for ocean oil spill classification. The research achievements and reference studies in regard to the features selection or bands selection have been obtained in previous related research field, such as hyperspectral band selection, not only by *J-M* distance method used in this study [43–46]. Especially in the case of that there are several complex lookalikes in the images, more effective feature selection methods are particularly of importance

for enhancing classification accuracy. It is noteworthy that main contribution of this paper is at the first proposing a scheme of jointly use of multiple fully Pol-SAR features for oil spill classification. Generally, in further oil spill classification experiments, which specific combination pattern of Pol-SAR features should be employed will be determined by test.

4.2. More Advanced Classifier Should Be Introduced or Developed for Further Promoting Ocean Oil Spill Classification Performance

From the pattern recognition perspective, selection/extraction of representative features of oil spill image is important for its classification. However, it is also a bottleneck to improving accuracy, due to variation of ocean environment when oil spill occurs. Therefore, learning features automatically from a remote sensing data set rather than using manually designed features, and then performing classification on the learned features, is an effective way to improve the accuracy of classification [47]. Deep learning theory was explicitly proposed by Hinton et al. [48] in 2006. It is a branch of machine learning based on a set of algorithms that attempt to model high level abstractions in data [49]. Compared with the traditional machine learning theories, the most significant difference of deep learning is emphasizing automatic feature learning from a huge data set through the organization of multi-layer neurons. In recent years, various deep learning architectures such as Deep Belief Networks (DBN) [50], Convolutional Neural Networks (CNN) [47], and Recurrent Neural Networks (RNN) [51] have been proposed and applied in speech, vision and image recognition and classification fields [52], they have been shown to produce state-of-the-art results in these domains, nevertheless, deep learning usually requires big data [53]. In deep learning techniques, CNN has achieved remarkable results in image classification, recognition, and other vision tasks [54–57]. Therefore, we believe CNN classification model will have a wide applying space in ocean oil spill image recognition and classification field, since increasing Pol-SAR datasets of ocean oil spill, such as RADARSAT-2, ENVISAT-ASAR, SIR-C/X SAR, and ALOS-PALSAR, allow a large amount of Pol-SAR data to be archived, and generate big Pol-SAR data of ocean oil spill. In the future research on ocean oil spill classification, we will be devoted to develop a CNN to achieve further enhancement of classification accuracy.

5. Conclusions

Oil spill pollution arising from ship or oil platform accidents represents a serious threat to the marine and coastal environment and ecosystems. Remote sensing observations are key to identify oil spills. To monitor such spill events from space, fully polarimetric synthetic aperture radar data has been increasingly employed in improving oil spill classification. In this study, the combined usage of multiple fully Pol-SAR features is exploited to classify sea oil spill in SAR imagery. Experiments, undertaken using two sets of RADARSAT-2 fully Pol-SAR data, confirm the effectiveness of the proposed approach. The main novelties that characterize this study can be summarized as follows.

- *J-M* distance index method is beneficial to select the fully Pol-SAR features. μ, H, *span*, P, and $\overline{\alpha}$ are selected in this study. Strong contrast degree of gray level of pixels between oil spill and water illustrates the selected features have good separability of oil spill and seawater.
- Jointly using multiple fully Pol-SAR features shows better classification performance of oil spill and seawater, compared with the classification results of only using single fully Pol-SAR feature.
- We build a more robust WNN classifier through setting optimal initial values of the network for oil spill classification. The experimental results demonstrate that the optimized WNN classifier can promote the classification performance largely, compared to an un-optimized WNN classifier.
- Since both the combined usage of fully Pol-SAR features and an optimized WNN classifier can improve classification performance, it proves the effectiveness and applicableness of the proposed method for ocean oil spill classification.

Acknowledgments: This work is supported by the National Science Foundation of China (61371189). Oil gas/Hydrocarbon detection and evaluation technology based on marine remote sensing gravity and magnetic, electric technology (2014A-0107). Oil Spill Detection based on Multi-source Remote Sensing data B16078). The views, opinions, and findings contained in this report are those of the authors, and should not be construed as official NOAA or US Government positions, policies, or decision. Thank Shiyong Yu who is with Department of Well Logging & Remote Sensing Technology, PetroChina Research Institute of Petroleum Exploration & Development for providing the help in the process of carrying out the experiment.

Author Contributions: Dongmei Song and Xiaofeng Li conceived and designed the experiments; Yaxiong Ding, Mingyu Xu performed the experiments; Biao Zhang analyzed the data; and Dongmei Song wrote the paper.

Conflicts of Interest: The authors declare no conflict of interest. The founding sponsors had no role in the design of the study; in the collection, analyses, or interpretation of data; in the writing of the manuscript, and in the decision to publish the results.

References

1. Garcia-Pineda, O.; Zimmer, B.; Howard, M.; Pichel, W.; Li, X.; MacDonald, I.R. Using SAR images to delineate ocean oil slicks with a texture-classifying neural network algorithm (tcnna). *Can. J. Remote Sens.* **2009**, *35*, 411–421. [CrossRef]
2. Migliaccio, M.; Gambardella, A.; Tranfaglia, M. SAR polarimetry to observe oil spills. *IEEE Trans. Geosci. Remote Sens.* **2007**, *45*, 506–511. [CrossRef]
3. Hu, C.; Li, X.; Pichel, W.G.; Muller karger, F.E. Detection of natural oil slicks in the NW gulf of Mexico using Modis imagery. *Geophys. Res. Lett.* **2009**, *36*. [CrossRef]
4. Liu, P.; Zhao, C.; Li, X.; He, M.; Pichel, W.G. Identification of ocean oil spills in SAR imagery based on fuzzy logic algorithm. *Int. J. Remote Sens.* **2010**, *31*, 4819–4833. [CrossRef]
5. Robinson, I.S. *Measuring the Ocean from Space—The Principles and Methods of Satellite Oceanography*; Springer: Berlin/Heidelberg, Germany, 2004; pp. 178–179.
6. Cheng, Y.; Li, X.; Xu, Q.; Garcia-Pineda, O.; Andersen, O.B.; Pichel, W.G. SAR observation and model tracking of an oil spill event in coastal waters. *Mar. Pollut. Bull.* **2011**, *62*, 350–363. [CrossRef] [PubMed]
7. Migliaccio, M.; Nunziata, F.; Gambardella, A. On the co-polarized phase difference for oil spill observation. *Int. J. Remote Sens.* **2009**, *30*, 1587–1602. [CrossRef]
8. Skrunes, S.; Brekke, C.; Eltoft, T. Characterization of marine surface slicks by Radarsat-2 multi polarization features. *IEEE Trans. Geosci. Remote Sens.* **2014**, *52*, 5302–5319. [CrossRef]
9. Li, X.; Li, C.; Yang, Z.; Pichel, W. SAR imaging of ocean surface oil seep trajectories induced by near inertial oscillation. *Remote Sens. Environ.* **2013**, *130*, 182–187. [CrossRef]
10. Garciapineda, O.; Macdonald, I.R.; Li, X.; Jackson, C.R.; Pichel, W.G. Oil spill mapping and measurement in the Gulf of Mexico with textural classifier neural network algorithm (tcnna). *IEEE J. Sel. Top. Appl. Earth Observ. Remote Sens.* **2013**, *6*, 2517–2525. [CrossRef]
11. Xu, Q.; Li, X.; Wei, Y.; Tang, Z.; Cheng, Y.; Pichel, W.G. Satellite observations and modeling of oil spill trajectories in the Bohai Sea. *Mar. Pollut. Bull.* **2013**, *71*, 107–116. [CrossRef] [PubMed]
12. Cheng, Y.; Liu, B.; Li, X.; Nunziata, F.; Xu, Q.; Ding, X.; Migliaccio, M.; Pichel, W.G. Monitoring of oil spill trajectories with Cosmo-Skymed X-band SAR images and model simulation. *IEEE J. Sel. Top. Appl. Earth Observ. Remote Sens.* **2014**, *7*, 2895–2901. [CrossRef]
13. Kim, T.S.; Park, K.A.; Li, X.; Lee, M.; Hong, S.; Lyu, S.J.; Nam, S. Detection of the Hebei spirit oil spill on SAR imagery and its temporal evolution in a coastal region of the Yellow sea. *Adv. Space Res.* **2015**, *56*, 1079–1093. [CrossRef]
14. Migliaccio, M.; Nunziata, F.; Montuori, A.; Li, X.; Pichel, W.G. A multifrequency polarimetric SAR processing chain to observe oil fields in the Gulf of Mexico. *IEEE Trans. Geosci. Remote Sens.* **2011**, *49*, 4729–4737. [CrossRef]
15. Zhang, B.; Perrie, W.; Li, X.; Pichel, W.G. Mapping sea surface oil slicks using Radarsat-2 quad-polarization SAR image. *Geophys. Res. Lett.* **2011**, *38*, 415–421. [CrossRef]
16. Liu, P.; Li, X.; Qu, J.J.; Wang, W.; Zhao, C.; Pichel, W.G. Oil spill detection with fully polarimetric UAVSAR data. *Mar. Pollut. Bull.* **2011**, *62*, 2611–2618. [CrossRef] [PubMed]
17. Migliaccio, M.; Nunziata, F.; Brown, C.E.; Holt, B.; Li, X.; Pichel, W.G.; Shimada, M. Polarimetric synthetic aperture radar utilized to track oil spills. *Eos Trans. Am. Geophys. Union* **2013**, *93*, 161–162. [CrossRef]

18. Nunziata, F.; Migliaccio, M.; Li, X. Sea oil slick observation using hybrid-polarity SAR architecture. *IEEE J. Ocean. Eng.* **2015**, *40*, 426–440. [CrossRef]
19. Buono, A.; Nunziata, F.; Migliaccio, M.; Li, X. Polarimetric analysis of compact-polarimetry SAR architectures for sea oil slick observation. *IEEE Trans. Geosci. Remote Sens.* **2016**, *54*, 5862–5874. [CrossRef]
20. Zhang, B.; Li, X.; Perrie, W.; Garcia-Pineda, O. Compact polarimetric synthetic aperture radar for marine oil platform and slick detection. *IEEE Trans. Geosci. Remote Sens.* **2017**, *55*, 1–17. [CrossRef]
21. Nunziata, F.; Migliaccio, M.; Gambardella, A. Pedestal height for sea oil slick observation. *IET Radar Sonar Navig.* **2011**, *5*, 103–110. [CrossRef]
22. Shirvany, R.; Chabert, M.; Tourneret, J.Y. Ship and oil-spill detection using the degree of polarization in linear and Hybrid/Compact Dual-Pol SAR. *IEEE J. Sel. Top. Appl. Earth Observ. Remote Sens.* **2012**, *5*, 885–892. [CrossRef]
23. Zhang, Y.; Li, Y.; Liang, X.S.; Tsou, J. Comparison of oil spill classifications using fully and compact polarimetric SAR Images. *Appl. Sci.* **2017**, *7*, 193–214. [CrossRef]
24. Migliaccio, M.; Gambardella, A.; Nunziata, F.; Shimada, M.; Isoguchi, O. The PALSAR polarimetric mode for sea oil slick observation. *IEEE Trans. Geosci. Remote Sens.* **2009**, *47*, 4032–4041. [CrossRef]
25. Minchew, B.; Jones, C.E.; Holt, B. Polarimetric analysis of backscatter from the deepwater horizon oil spill using l-band synthetic aperture radar. *IEEE Trans. Geosci. Remote Sens.* **2012**, *50*, 3812–3830. [CrossRef]
26. Migliaccio, M.; Nunziata, F.; Buono, A. SAR polarimetry for sea oil slick observation. *Int. J. Remote Sens.* **2015**, *36*, 3243–3273. [CrossRef]
27. Singha, S.; Bellerby, T.J.; Trieschmann, O. In detection and classification of oil spill and look-alike spots from SAR imagery using an artificial neural network. *IEEE Trans. Geosci. Remote Sens.* **2012**, *53*, 5630–5633.
28. Collingwood, A.; Treitz, P.; Charbonneau, F.; Atkinson, D. Artificial neural network modeling of high arctic phytomass using synthetic aperture radar and multispectral data. *Remote Sens.* **2014**, *6*, 2134–2153. [CrossRef]
29. Taravat, A.; Proud, S.; Peronaci, S.; del Frate, F.; Oppelt, N. Multilayer perceptron neural networks model for meteos at second generation SEVIRI daytime cloud masking. *Remote Sens.* **2015**, *7*, 1529–1539. [CrossRef]
30. Heermann, P.D.; Khazenie, N. Classification of multispectral remote sensing data using a back-propagation neural network. *IEEE Trans. Geosci. Remote Sens.* **1992**, *30*, 81–88. [CrossRef]
31. Zuo, L. Supervised classification of multispectral remote sensing image using BP neural network. *J. Infrared Millim. Waves* **1998**, *17*, 153–156.
32. Li, J.; Du, Q.; Li, Y. An efficient radial basis function neural network for hyperspectral remote sensing image classification. *Soft Comput.* **2015**, *20*, 1–7. [CrossRef]
33. Karayiannis, N.B.; Venetsanopoulos, A.N. Fast learning algorithms for neural networks. *IEEE Trans. Circuits Syst. II Analog Digit. Signal Process.* **1992**, *39*, 453–474. [CrossRef]
34. Benediktsson, J.A.; Swain, P.H.; Ersoy, O.K. Conjugate-gradient neural networks in classification of multisource and very-high-dimensional remote sensing data. *Int. J. Remote Sens.* **1993**, *14*, 2883–2903. [CrossRef]
35. Jin, C. Structure modality of the error function for feed forward neural networks. *J. Comput. Res. Dev.* **2003**, *40*, 913–917.
36. Zhang, Q.G.; Benveniste, A. A wavelet networks. *IEEE Trans. Neural Netw.* **1992**, *3*, 889–898. [CrossRef] [PubMed]
37. Song, D.; Chen, S.; Ma, Y.; Shen, C.; Zhang, Y. Impact of different saturation encoding modes on object classification using a BP wavelet neural network. *Int. J. Remote Sens.* **2014**, *35*, 7878–7897. [CrossRef]
38. Jin, Y.; Chen, G.; Liu, H. Fault diagnosis of analog circuit based on BP wavelet neural network. *Meas. Control. Technol.* **2007**, *26*, 64–69.
39. Song, D.; Zhang, Y.; Shan, X. "Over-Learning" phenomenon of wavelet neural networks in remote sensing image classifications with different entropy error functions. *Entropy* **2017**, *19*, 101–119. [CrossRef]
40. Song, D.; Liu, B. Hyperspectral data spectrum and texture band selection based on the subspace-rough set method. *Int. J. Remote Sens.* **2015**, *36*, 2113–2128. [CrossRef]
41. Hara, Y.; Atkins, R.; Shin, R. Application of neural networks for sea ice classification in Polarimetric SAR images. *IEEE Trans. Geosci. Remote Sens.* **1995**, *33*, 740–748. [CrossRef]
42. Soh, L.; Tsatsoulis, C. Texture Analysis of SAR sea ice imagery using gray level co-occurrence matrices. *IEEE Trans. Geosci. Remote Sens.* **1999**, *37*, 780–795. [CrossRef]

43. Dabboor, M.; Howell, S.; Shokr, M.; Yackel, J. The jeffries–matusita distance for the case of complex wishart distribution as a separability criterion for fully polarimetric SAR data. *Int. J. Remote Sens.* **2014**, *35*, 6859–6873.
44. Marçal, A.; Borges, J.S.; Gomes, J.A.; Costa, J.F.P.D. Land cover update by supervised classification of segmented aster images. *Int. J. Remote Sens.* **2005**, *26*, 1347–1362. [CrossRef]
45. Chen, M. Optimal bands selection of remote sensing image based on core attribute of rough set theory. *J. Ningde Teach. Coll. (Nat. Sci.)* **2016**, *18*, 378–380.
46. Asl, M.G.; Mobasheri, M.R.; Mojaradi, B. Unsupervised feature selection using geometrical measures in prototype space for hyperspectral imagery. *IEEE Trans. Geosci. Remote Sens.* **2014**, *52*, 3774–3787.
47. Fu, G.; Liu, C.; Zhou, R. Classification for high resolution remote sensing imagery using a fully convolutional network. *Remote Sens.* **2017**, *9*, 2–21. [CrossRef]
48. Hinton, G.; Osindero, S.; Welling, M.; Teh, Y.W. Unsupervised discovery of nonlinear structure using contrastive backpropagation. *Cogn. Sci.* **2006**, *30*, 725–732. [CrossRef] [PubMed]
49. Mnih, V.; Kavukcuoglu, K.; Silver, D.; Rusu, A.A.; Veness, J.; Bellemare, M.G.; Graves, A.; Riedmiller, M.; Fidjeland, A.K.; Ostrovski, G.; et al. Human-level control through deep reinforcement learning. *Nature* **2015**, *518*, 529–533. [CrossRef] [PubMed]
50. Hinton, G.E.; Osindero, S.; Teh, Y.W. A fast learning algorithm for deep belief nets. *Neural Comput.* **2014**, *18*, 1527–1554. [CrossRef] [PubMed]
51. Graves, A.; Liwicki, M.; Fernandez, S.; Bertolami, R.; Bunke, H.; Schmidhuber, J. A novel connectionist system for improved unconstrained handwriting recognition. *IEEE Trans. Pattern Anal. Mach. Intell.* **2009**, *31*, 855–868. [CrossRef] [PubMed]
52. Wu, H.; Prasad, S. Convolutional recurrent neural networks for hyperspectral data classification. *Remote Sens.* **2017**, *9*, 298. [CrossRef]
53. Chen, Y.; Jiang, H.; Li, C.; Jia, X.; Ghamisi, P. Deep feature extraction and classification of hyperspectral images based on convolutional neural networks. *IEEE Trans. Geosci. Remote Sens.* **2016**, *54*, 6232–6250. [CrossRef]
54. Ghamisi, P.; Chen, Y.; Zhu, X.X. A self-improving convolution neural network for the classification of hyperspectral data. *IEEE Geosci. Remote Sens. Lett.* **2016**, *13*, 1537–1541. [CrossRef]
55. Maggiori, E.; Tarabalka, Y.; Charpiat, G.; Alliez, P. Convolutional neural networks for large-scale remote-sensing image classification. *IEEE Trans. Geosci. Remote Sens.* **2016**, *55*, 1–13. [CrossRef]
56. Li, Y.; Xie, W.; Li, H. Hyperspectral image reconstruction by deep convolutional neural network for classification. *Pattern Recogn.* **2016**, *63*, 371–383. [CrossRef]
57. Nogueira, K.; Penatti, O.A.B.; Santos, J.A.D. Towards better exploiting convolutional neural networks for remote sensing scene classification. *Pattern Recogn.* **2017**, *61*, 539–556. [CrossRef]

© 2017 by the authors. Licensee MDPI, Basel, Switzerland. This article is an open access article distributed under the terms and conditions of the Creative Commons Attribution (CC BY) license (http://creativecommons.org/licenses/by/4.0/).